OPEN ACCESS
IOP Publishing
Journal of Physics D: Applied Physics
J. Phys. D: Appl. Phys. **57** (2024) 355301 (13pp)
https://doi.org/10.1088/1361-6463/ad5021

# Nanoparticle ZnS:Ag/$^{6}$LiF—a new high count rate neutron scintillator with pulse shape discrimination

**Sarah E Mann[1,2], Erik M Schooneveld[1], Nigel J Rhodes[1], Giacomo Mauri[1], Dong Liu[3] and G Jeff Sykora[1,*]**

[1] Science and Technology Facilities Council, ISIS Neutron and Muon Source, Rutherford Appleton Laboratory, Harwell Oxford OX11 0QX, United Kingdom
[2] University of Bristol, School of Physics, Bristol BS8 1TH, United Kingdom
[3] Department of Engineering Science, University of Oxford, Oxford OX1 3PJ, United Kingdom

E-mail: jeff.sykora@stfc.ac.uk

Received 22 March 2024, revised 22 April 2024
Accepted for publication 24 May 2024
Published 6 June 2024

**Abstract**

A neutron sensitive scintillator employing nanoparticles of ZnS:Ag has been developed for the first time. Pulse shape differences between neutron and gamma signals were observed in this material and neutron-gamma discrimination was applied. With initial signal processing parameters, gamma sensitivities of $8.5 \times 10^{-6}$ to $^{60}$Co gammas were achieved. The average primary decay of neutron scintillation in nanoparticle ZnS:Ag/$^{6}$LiF was measured to be 18ns, and afterglow was significantly suppressed in comparison to standard ZnS:Ag/$^{6}$LiF scintillators that employ micron sized ZnS:Ag. Fast decay times and minimal afterglow indicate potential for use in high count rate capability applications. Prospective count rate capabilities were investigated here as proof of concept, with rates of 1.12Mcps measured for a single readout channel with less than 3.5% count loss. This is approximately 70 times greater than the count rate capability of the current standard ZnS:Ag/$^{6}$LiF scintillation detectors. With improvements to signal processing and scintillator composition, nanoparticle ZnS:Ag/$^{6}$LiF could be a promising candidate for future high rate capability neutron detectors.

Keywords: nanoparticle scintillator, neutron detection, pulse shape discrimination, ZnS:Ag, high count rate capability, neutron scattering

## 1. Introduction

Effective neutron detectors are essential in a wide range of industries including nuclear energy, nuclear security/non-proliferation, radiation monitoring, and neutron scattering for materials science research [1, 2]. At neutron scattering facilities a range of neutron techniques including diffraction, reflectometry, spectroscopy, and imaging are employed across different instruments in order to study the structure and dynamics of materials [3]. Current major neutron scattering facilities include ISIS Neutron and Muon Source in the UK, Institut Laue-Langevin in France, National Institute of Standards and Technology and Spallation Neutron Source (SNS) in the USA, Japan Proton Accelerator Research Complex, and the China SNS [4–9]. The coming decade will see the beginning of operation at the European Spallation Source in Sweden, which promises to be the world's most

* Author to whom any correspondence should be addressed.

powerful neutron source [10]. Looking further ahead, a second target station will be constructed at the SNS and designs are underway for the UK's next generation neutron and muon source, ISIS-II [11–13].

The demands for detectors at neutron scattering facilities are particularly rigorous as detector properties have a direct impact on the achievable science output. Specific requirements vary depending on technique and instrument, therefore the flexibility to tailor detector design to unique instrument requirements is critical. In general, most detectors at scattering facilities are required to have high neutron detection efficiency (up to 80% at thermal wavelengths), high count rate capability (up to 1 M counts per second (cps) $cm^{-2}$), low gamma sensitivity (fewer than 1 in $10^5$ gammas counted), low background rate (down to 0.1 counts $hr^{-1}cm^{-2}$) and fine (sub-millimetre) position resolution [2, 14–17]. Large area and solid angle coverage (up to tens of $m^2$, close to $4\pi$) is also often required [18–20].

Scintillation detectors are increasingly being used at scattering facilities as the global shortage, and correlated expense, of $^3$He limits the development of new large area $^3$He gas detectors [21, 22]. Scintillation detectors offer an affordable alternative to gas detectors; they can be designed to cover complex geometries or large areas. Most scintillation detectors at scattering facilities employ either cerium doped lithium glass scintillators (e.g. GS20) or ZnS:Ag/$^6$LiF, which both possess notable limitations [23–30].

Detectors employing lithium glass scintillators are disadvantaged by the inherent lack of pulse shape discrimination (PSD) capabilities. PSD is a fundamental property of some scintillators that allows for the separation of signals based on the ionisation density of different types of radiation. Different scintillators exhibit PSD to different extents. For example, neutron and gamma signals have characteristically different decay times in ZnS:Ag/$^6$LiF therefore effective rejection of gamma signals can be carried out in signal processing. As lithium glass scintillators have no fundamental pulse shape differences, gamma rejection must be done entirely using signal amplitude which limits gamma sensitivities to $\sim 10^{-3}$ when high neutron detection efficiency is required [30]. As a result, lithium glass scintillators are not appropriate for various neutron techniques. Instead, they are predominately used for applications where low gamma sensitivities are not as critical, such as beamline monitors, as well as in cases where gamma rejection is sacrificed to meet other specifications [15].

The main drawback of traditional ZnS:Ag/$^6$LiF scintillation detectors is that their count rate capability is inherently limited by the scintillation timing properties [31]. While absolute values vary with signal processing techniques, in ZnS:Ag/$^6$LiF detectors at ISIS, rate limitations of 10% deadtiming at 16 kcps and saturation at 35 kcps per readout channel are typically seen [32].

With continual upgrades to existing neutron scattering facilities and the development of new ones, the requirements on neutron detectors are increasing. New facilities may offer neutron fluxes orders of magnitude higher than at present and the current standard of neutron detectors will not be able to cope. Therefore, the development of affordable, large area neutron detectors with excellent gamma rejection and high count rate capability is a growing priority.

The count rate limitation in ZnS:Ag/$^6$LiF detectors is the result of the material's inherent scintillation properties. ZnS:Ag has broadband luminescence centred at 450 nm and is one of the brightest known inorganic scintillators. ZnS:Ag/$^6$LiF has an approximate light yield of 160 000 photons per neutron and 75 000 photons per MeV for gamma interactions [33]. Prompt scintillation in ZnS:Ag occurs when excited electrons and holes recombine at the silver luminescence centre directly after ionisation. This takes place on relatively fast timescales, giving ZnS:Ag a primary decay of 180 ns [31]. However, ZnS:Ag has a large number of defects in the lattice structure which act as electron and hole traps and can result in long lifetime luminescence (afterglow). Electrons or holes that become trapped after ionisation can radiatively recombine when they overcome potential barriers by thermal excitation or quantum tunnelling [34]. These processes extend emission for milliseconds after excitation. In combination with the intrinsic large dynamic range in light output from ZnS:Ag/$^6$LiF scintillator, this afterglow results in unavoidable count rate limitations. To facilitate the development of the next generation of high rate capability neutron detectors, there is an ongoing search for low afterglow alternatives to ZnS:Ag scintillator that possess excellent PSD capabilities. Various fast scintillators are under development and investigation, however there are currently no commercially available scintillators that meet all the requirements for use in neutron scattering detectors [32, 35, 36].

In previous work, nanoparticles of ZnS:Ag were demonstrated to have fast scintillation properties that indicated the material may have promise as a low afterglow alternative to commercial bulk ZnS:Ag [37]. When excited by alpha radiation, the average decay to 1% was measured to be approximately 20 times faster in nanoparticle ZnS:Ag than in the bulk counterpart. While other researchers have explored the use of ZnS:Ag nanoparticles as alpha particle detectors [38, 39], the neutron response has not been previously investigated. The present work demonstrates the first thermal neutron sensitive nanoparticle ZnS:Ag/$^6$LiF scintillator. The potential of this nanoparticle scintillator for use in neutron scattering detectors is explored; pulse shape differences between neutron and gamma and the prospective count rate capabilities are shown here for the first time.

## 2. Materials and methods

### 2.1. Synthesis and scintillator screen composition

Nanoparticles of ZnS:Ag were produced using a hydrothermal synthesis method, as described by several researches [39–41]. Reagents of thiourea (>99%), anhydrous zinc acetate (>99.99%) and silver nitrate (>99%) from Sigma Aldrich were used without further purification. The reagents were mixed in a molar ratio of Zn:S:Ag $= 1:1:5\times10^{-4}$ and heated in a Teflon lined autoclave at 220 °C for 12 h. The resulting precipitate was extracted and washed four times, alternating between solvents of de-ionised water and ethanol. Each

time the precipitate was separated from solution by centrifuging for 10 min at 6000 rpm. Finally, the powder was dried in a vacuum oven at 30 °C.

$^{6}$Li has a thermal neutron absorption cross section of 940 barns [42] and decays following a process described in equation (1) to produce an alpha and triton. These charged particles excite ZnS:Ag causing the emission of light which is detected, indicating the interaction of ionising radiation in the scintillator

$$n + {}^{6}\mathrm{Li} \rightarrow {}^{4}\mathrm{He} + {}^{3}\mathrm{H} + 4.79\ \mathrm{MeV}. \quad (1)$$

A scintillator screen was fabricated by mixing $^{6}$Li enriched LiF powder (95% enrichment) with the synthesised ZnS:Ag nanoparticles and transparent epoxy binder (Loctite EA 9483) and casting the mixture in a silicon mould. $^{6}$LiF powder, ZnS:Ag nanoparticles, and binder were used in a ratio of 1:3:3 by mass. A similar scintillator screen was produced using commercially available ZnS:Ag powder (NC2) with median grain size of 8 $\mu$m from Phosphor Technology. Both scintillator screens had dimensions of 2 cm×2 cm and were sanded to have a uniform thickness of 0.85 mm. For simplicity, the scintillator screens made using ZnS:Ag nanoparticle and micrometer sized commercial particles will be referred to henceforth as the 'nanoscintillator' and 'microscintillator' respectively. The ZnS:Ag/$^{6}$LiF nanoscintillator and microscintillator screens are shown in figures 1(a) and (b) respectively. Figures 1(c) and (d) shows the same screens illuminated by 340 nm light. While standard ZnS:Ag has bright blue emission, the nanoscintillator exhibits photoluminescence peaked at yellow wavelengths.

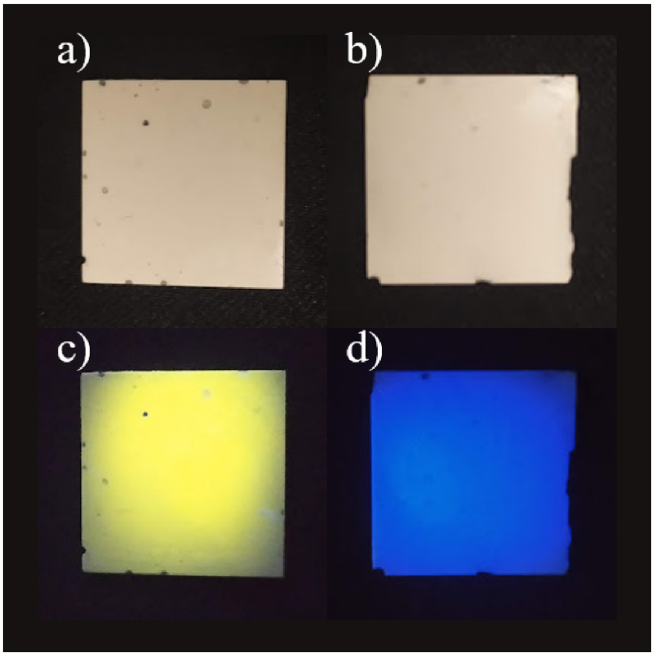


**Figure 1.** Photographs of ZnS:Ag/$^{6}$LiF scintillator screens made from synthesised nanoparticles (referred to as 'nanoscintillator') shown in (a), (c), and standard commercial ZnS:Ag phosphor with micro-size particles (referred to as 'microscintillator') shown in (b), (d). Images (a) and (b) were acquired with ambient lighting, while (c) and (d) show the screens illuminated by 340 nm UV excitation.

### 2.2. Experimental methods

The phase and size of the synthesised nanopowder were verified using x-ray diffraction (XRD) measurements on a Rigaku Miniflex diffractometer. X-ray diffraction was also performed on Phosphor Technologies' ZnS:Ag powder (NC2) for comparison.

Excitation-Emission spectra were acquired using an Edinburgh Instruments FLS1000 Spectrometer. A 400 nm high pass filter was positioned in the emission path to reduce the effect of second order excitation features. Measurements without this filter verified no emission features were excluded as a consequence.

Neutron detector prototypes were assembled by grease coupling the nanoscintillator or microscintillator screen to a photomultiplier tube (PMT). In either case, the scintillator was covered by a reflective Teflon cap to increase light collection. A 16-channel bi-alkali PMT produced by Hamamatsu (Type H8711–300 mod) was adopted for the measurements where the PMT was effectively used as a single anode PMT with an active area of 16 mm×16 mm as the signal from all 16 channels was combined into one readout channel. The analogue signal from the PMT was collected using a picoscope 5444d series in 12-bit mode and using a sample period of 4 ns. Signals were post-processed using LabView software.

The timing properties of scintillation and neutron-gamma discrimination capability were investigated using low rate sources. Gamma measurements were performed by exposing the detector to a $^{60}$Co source with activity of $4.4 \times 10^{6}$ Bq ($3000\gamma\ \mathrm{s}^{-1}\mathrm{cm}^{-2}$). A moderated $^{241}$Am-Be neutron/gamma source with rate ∼100n $\mathrm{s}^{-1}\mathrm{cm}^{-2}$ was used to study the neutron response. This source emits neutrons over a broad spectrum with a mean effective wavelength of 1.2 Å (57 meV). For the source tests the incident rate was relatively low, so individual traces were saved when the analogue signal surpassed a trigger threshold of approximately 6 single photons.

Performance at high neutron flux was studied on the EMMA and CRISP beamlines on Target Station 1 at ISIS [43, 44]. EMMA was used to study neutron gamma discrimination in neutron scattering, while CRISP was used to investigate the count rate capability of the detector. ISIS is a short pulse neutron source which operates at a frequency of 50 Hz (period of 20 ms) [45]. Both EMMA and CRISP employ Inconel alloy choppers which operate at 50 Hz to remove the prompt $t_0$ (the time at which the proton beam hits the target) gammas and fast neutrons from the respective spectra.

EMMA views a room temperature water moderator which produces a neutron spectrum with a Maxwellian peak located at 1 Å. The neutron flux in this peak is approximately $1 \times 10^{6}$ n $\mathrm{s}^{-1}\mathrm{cm}^{-2}$. Gamma rejection capabilities in a neutron scattering setting were studied on EMMA by shielding the detector from incident neutrons with $B_4C$ and using a Cd sheet to create a large gamma flood on the detector. Details of this experimental

set up are described in section 3.2.2, together with the results of the measurements.

CRISP is a neutron reflectometer that views a liquid hydrogen moderator which has a nominal temperature of 22 K. It was chosen for rate capability measurements as the peak flux (at $\lambda = 2.6$ Å) is notably higher than on EMMA: approximately $6\times10^6$ n $s^{-1}cm^{-2}$ depending on the beam current and moderator temperature. The detector was placed in the sample position at a distance of 10.23 m from the moderator. Incident rate on the detector was controlled using the instrument's neutron attenuating slits, which are made of Cd and $B_4C$.

For these beamline measurements, 10–16 ms traces were recorded when triggered by the synchrotron $t_0$ pulse. Individual neutron events in each frame were identified in post processing. Details of the signal processing techniques used are described in section 3.2.

## 3. Results and discussion

### 3.1. Nanoparticle scintillator properties

The XRD spectra of both types of powder, i.e. the synthesized ZnS:Ag nanoparticles used to create the nanoscintillator (black), and commercially available micron sized ZnS:Ag powder used in the fabrication of the microscintillator (blue), are shown in figure 2. Peak positions confirm that cubic ZnS was formed in both cases, and the (*hkl*) planes corresponding to the dominant peaks are labelled. The width of the XRD peaks was used to determine the size of the nanocrystals through the Scherrer equation [46], assuming broadening is dominated by particle size. Curve fitting to the data in figure 2 indicates the synthesised nanoparticles have an average crystallite size of $5.2 \pm 0.9$ nm. A shift in peak positions with increasing angle is observed indicating a small contraction ($\sim$1.0%) of the cubic ZnS lattice parameter in the synthesised nanoparticles.

A photoluminescence (PL) excitation-emission map of the nanoscintillator is shown in figure 3. PL is broadband and peaked at excitation and emission wavelengths of 356 nm and 568 nm respectively. The PL of commercial ZnS:Ag is reported in previous works; excitation and emission spectra of ZnS:Ag (NC2) powder are shown in [37], and a full excitation-emission map of ZnS:Ag/$^6$LiF scintillator is presented in [31]. The nanoscintillator emission is shifted to significantly longer wavelengths with respect to the microscintillator, which has PL peaked at 450 nm. The peak emission shift corresponds to a median energy transition of 2.18 eV, which is 0.575 eV smaller than the standard microscintillator. Excitation is also peaked at a slightly longer wavelength in the nanoscintillator than in the microscintillator, 356 nm compared to 340 nm. The excitation spectrum suggests a bandgap of approximately 3.18 eV, which is 0.2 eV smaller than the microscintillator [31]. Differences in the PL spectra between the nanoscintillator and microscintillator indicate different luminescence mechanisms are occurring in the two materials. The emission shift seen in the nanoparticles is not due to quantum confinement as this would result in emission at shorter wavelengths. Instead the luminescence behaviour is likely dominated by surface defects, which become more significant with a larger surface-to-volume ratio.

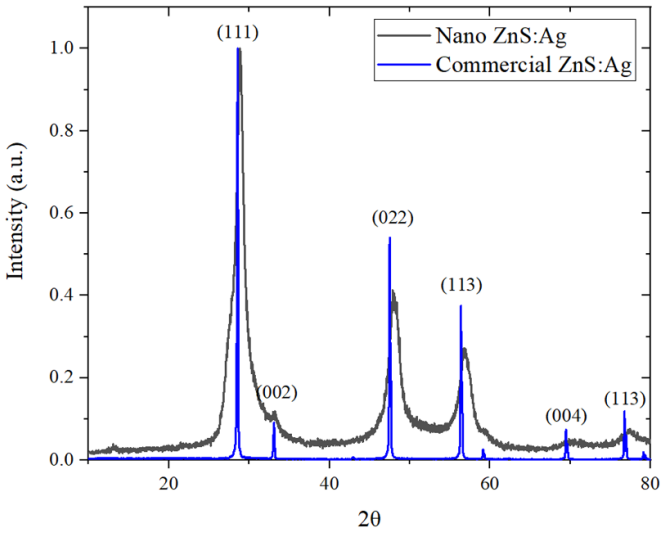


**Figure 2.** X-ray diffraction spectra measured for synthesised nanopowder (black) and commercial micron sized ZnS:Ag powder (blue). Labels indicate (*hkl*) planes corresponding to main peaks.

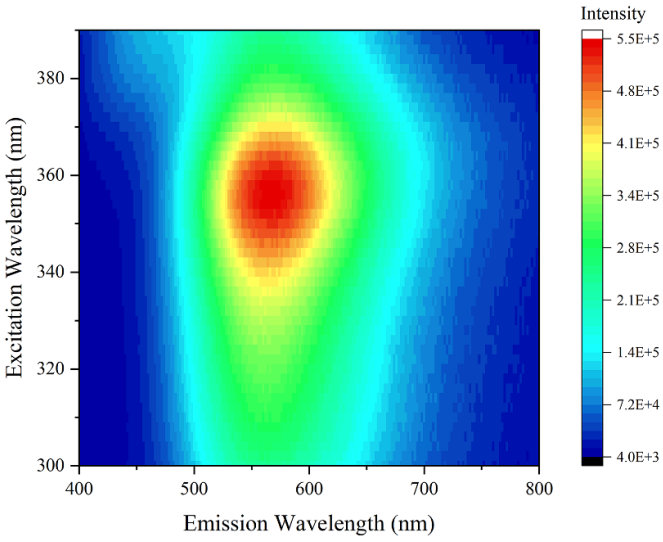


**Figure 3.** Excitation-emission spectra for nanoparticle ZnS:Ag/$^6$LiF scintillator.

Figure 4 shows the quantum efficiency of the PMT (black dashed line) alongside the normalised PL emission from the nanoscintillator at 356 nm excitation (red solid line). Poor overlap between the emission and collection wavelengths is evident. The convolution of the two spectra in figure 4 indicates that approximately 11% of the emitted light can be collected by the PMT. This is in contrast to approximately 33% of emitted light that can be collected from the blue emitting microscintillator. To try and overcome this issue, a PMT with a multi-alkali cathode designed for enhanced efficiency at longer wavelengths was tested, however the data quality suffered due to increased sensitivity to thermal noise.

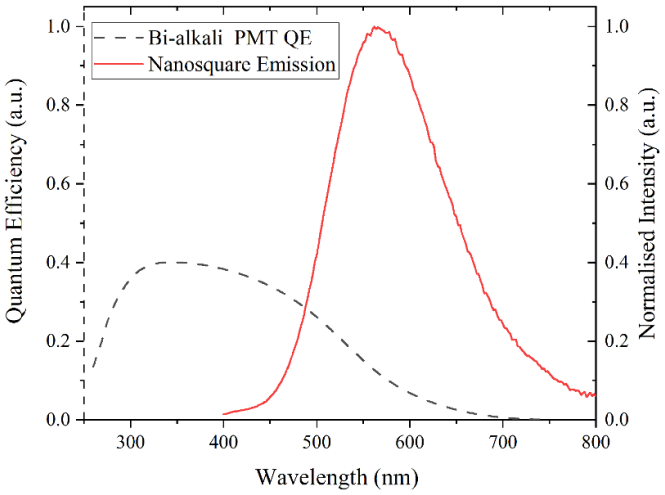


**Figure 4.** Quantum efficiency of the PMT used (black dashed line) and normalised PL emission from the nanoscintillator (red solid line), as a function of wavelength.

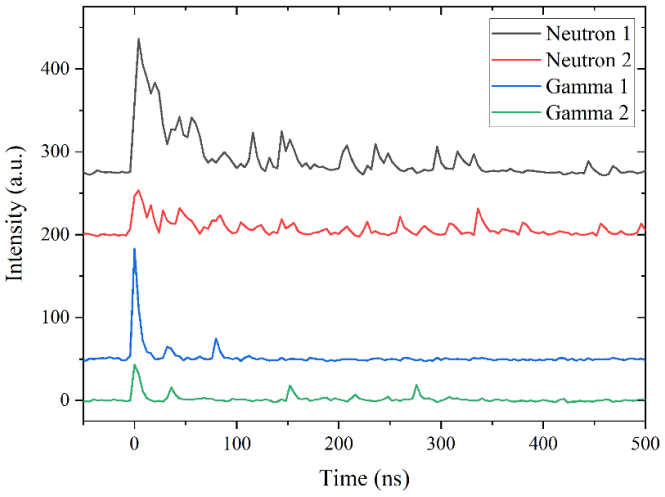


**Figure 5.** Typical analogue PMT signals recorded for gamma (blue and green) and neutron (red and black) events in the nanoscintillator. Signals are offset vertically for better visualisation.

### *3.2. Neutron-gamma discrimination*

*3.2.1. Pulse shape discrimination.* Typical analogue PMT signals recorded for gamma and neutron interactions in the nanoparticle scintillator system are depicted in figure 5. The large dynamic range of light output from neutron interactions can be seen by comparing the signals shown in red and black lines (Neutron 1 and Neutron 2 in figure 5). Dynamic range in light output arises as the total energy produced from the neutron absorption reaction (equation (1)) can be deposited in binder, lithium or scintillator particles. The brightest signals are produced when the triton and alpha particles deposit the majority of their energy in scintillator grains. The opacity of the scintillator also limits the total light output, therefore a neutron absorbed closest to the surface of the scintillator coupled to the PMT will produce a larger signal. As illustrated in figure 5, neutron and gamma signals cannot be distinguished by simply comparing pulse height. However, differences in the signal shape between neutron and gamma interactions are present which can be exploited to achieve PSD.

A PSD metric based on the integrated charge of a given signal, normalised to its maximum intensity was used to separate signals. This was calculated by integrating over the first 320 ns of signal and dividing by peak intensity as described in equation (2):

$$\mathrm{PSD} = \int_0^{320\ \mathrm{ns}} \frac{I(t)}{I_{\max}} \mathrm{dt}, \tag{2}$$

where $I$ is the intensity of the analogue PMT signal, and $I_{\max}$ the maximum intensity (pulse height).

Figure 6 shows PSD histograms produced using equation (2) when the nanoparticle scintillator detector was exposed to: (a) neutrons and gammas from the $^{241}$Am-Be source, and (b) gammas from the $^{60}$Co source described in section 2.2. In total, $1 \times 10^5$ events are included in figure 6(a). Traces were collected on the gamma source for a total exposure of 1 h, resulting in approximately $2 \times 10^5$ total events recorded in figure 6(b). Two distinct regions, with some overlap, are visible in the mixed radiation field. As the scintillator was directly coupled to the PMT, figures 6(a) and (b) both include direct interactions of gammas in the PMT. A set of measurements were carried out without the scintillator and these verified that the direct interactions have the time profile of the PMT's impulse response. These interactions generally have low pulse height ($<$0.1 V) and low PSD values ($<$2.5) so are therefore confined to the lower left corner of the PSD plots in figure 6. Separating PMT interactions from dimmer gamma scintillation events was not possible due to the fast decay within the impulse response time of the PMT. For the purpose of this work gamma interactions both in the PMT and scintillator are simply referred to as gamma events.

Figure 6(b) illustrates the detector response in a pure gamma field, confirming that events with large PSD, visible in figure 6(a), correspond to neutron signals. While neutron signals generally have a higher PSD value, a simple PSD cut does not provide the optimum separation between neutron and gamma signals due to significant overlap of the two regions. Depending on the PSD value used to separate neutrons from gammas, either a large number of neutrons would be rejected, or a large proportion of gammas erroneously counted as neutron events. The difficulty in separation is partially due to the large dynamic range of light output in ZnS:Ag/$^6$LiF scintillation signals, which is not sufficiently compensated for using this PSD technique.

To address the issue of large dynamic range, a signal processing and discrimination method that uses a filtered binary mask (FBM) technique was employed. This FBM method was based on the analogue signal processing techniques used in traditional ZnS:Ag/$^6$LiF detectors at ISIS and adjusted for the different signal types produced by the nanoparticle scintillators [31]. The FBM technique is illustrated in figure 7 and operates as follows: (1) discrete digital pulses were output when a threshold of approximately four photoelectrons was surpassed; (2) this digital signal was filtered by low and high

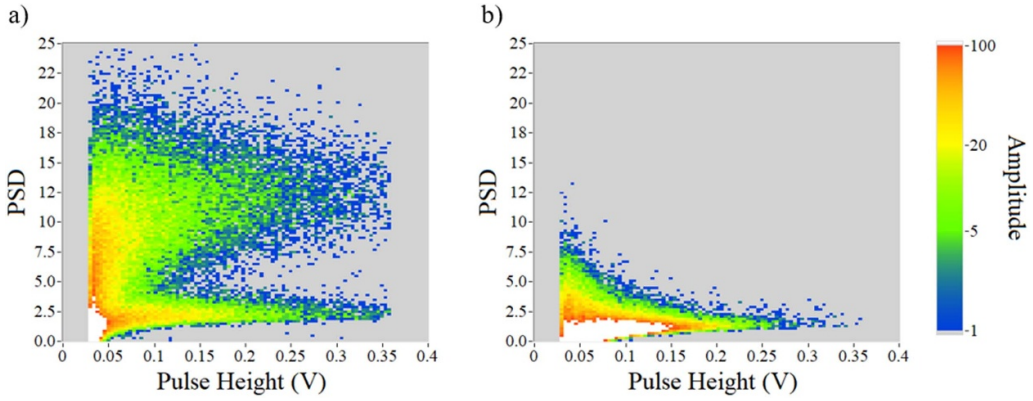


**Figure 6.** PSD histograms measured with ZnS:Ag/$^{6}$LiF nanoscintillator on (a) $^{241}$Am-Be neutron/gamma source and (b) $^{60}$Co gamma source.

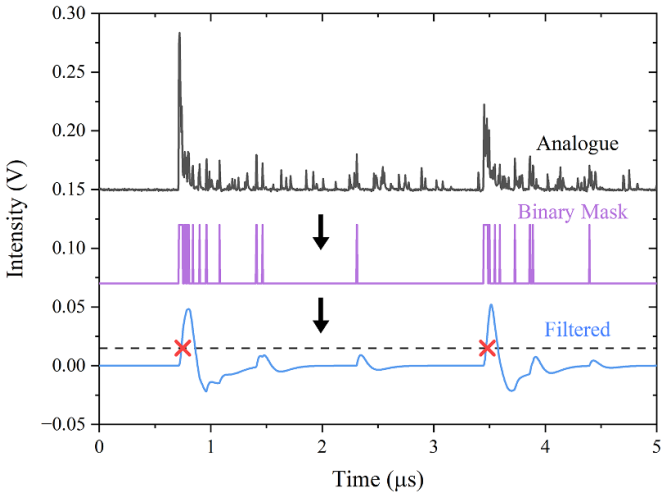


**Figure 7.** Illustration of the FBM technique used to identify neutrons. Analogue PMT signal (top, black) is converted into digital pulses (middle, purple) when a minimum binary mask threshold is surpassed. The digital signal is filtered by integrating and differentiating filters to produce the blue trace. Peaks above a given threshold with a minimum width are classified as neutrons, indicated by the red crosses.

pass infinite impulse response (IIR) Bessel filters consecutively; (3) peaks with a minimum width above a chosen acceptance threshold were identified and classified as neutron events. In figure 7 analogue PMT signal, binary pulses and filtered traces are shown by black, purple and blue traces respectively. Detected neutrons are indicated by red crosses.

There are a number of variables in the FBM technique, including binary mask threshold, filtration settings (number and type of filters, order, cut-off frequencies), discrimination threshold and peak width of the filtered signal. These factors are inter-dependent and cannot be optimised individually. Small changes to any of these properties can cause significant changes in detector performance. As such, the optimisation of the parameters can be tailored to performance requirements and will need further research. In order to determine reasonable signal processing parameters, the analogue and filtered signals of individual traces that could be clearly identified as neutrons or gammas were inspected. Bessel filters were chosen due to their smooth impulse response which does not introduce additional ringing to signals. The frequency of the high pass filter dictates the width of the filtered signal and therefore sets an upper limit on rate capability. A high pass frequency of 2 MHz was selected as this was suitably high to avoid introducing filtration dependent rate limitations in the current tests. The processing parameters that resulted in the best combination of low gamma sensitivity and high rate capability were selected, and are given in table 1. As these filtration parameters have not yet undergone full optimisation, the following results are intended as a first investigation to demonstrate the potential of nanoparticle ZnS:Ag/$^{6}$LiF, rather than the absolute limitations.

Figures 8(a) and (b) show the data from figure 6 with the FBM technique applied. This technique is reasonably effective at extracting the neutron signals from the gamma background, even without applying a PSD threshold. In comparison to figure 6(a), figure 8(a) shows predominantly the neutron region (high PSD values), with only a small tail of gamma events remaining. Figure 8(b) shows the events on the $^{60}$Co gamma source that were identified as neutrons using this technique. The majority of these are gamma interactions, incorrectly classified as neutrons. By inspecting figures 8(a) and (b), it can be seen that improved gamma rejection capabilities without significant loss of neutron detection efficiency can be obtained by applying a minimum PSD threshold. Figures 8(c) and (d) shows the events counted as neutrons when the SPC technique is combined with the normalised integrated charge discrimination technique. In this case the threshold was set at $\mathrm{PSD} = \int_0^{320\ \mathrm{ns}} \frac{I(t)}{I_{\max}} \mathrm{d}t > 4.0$.

Gamma sensitivity was determined using the events that were identified as neutrons by this signal processing when the detector was exposed to the $^{60}$Co gamma source. These are shown in figure 8(d). A small proportion of these events will be real neutron interactions, the primary source of these is scattering from the $^{241}$Am-Be source at the opposite end of the

**Table 1.** Signal processing parameters used to process measured signals and identify neutron events.

| | IIR Bessel Filter Cut-Off Frequencies (MHz) | | Discrimination Parameters | |
|---|---|---|---|---|
| Binary Mask Threshold (mV) | Low Pass | High Pass | Threshold (mV) | Width (ns) |
| 20 | 2.5 (2nd order) | 2.0 (1st order) | 15 | 60 |

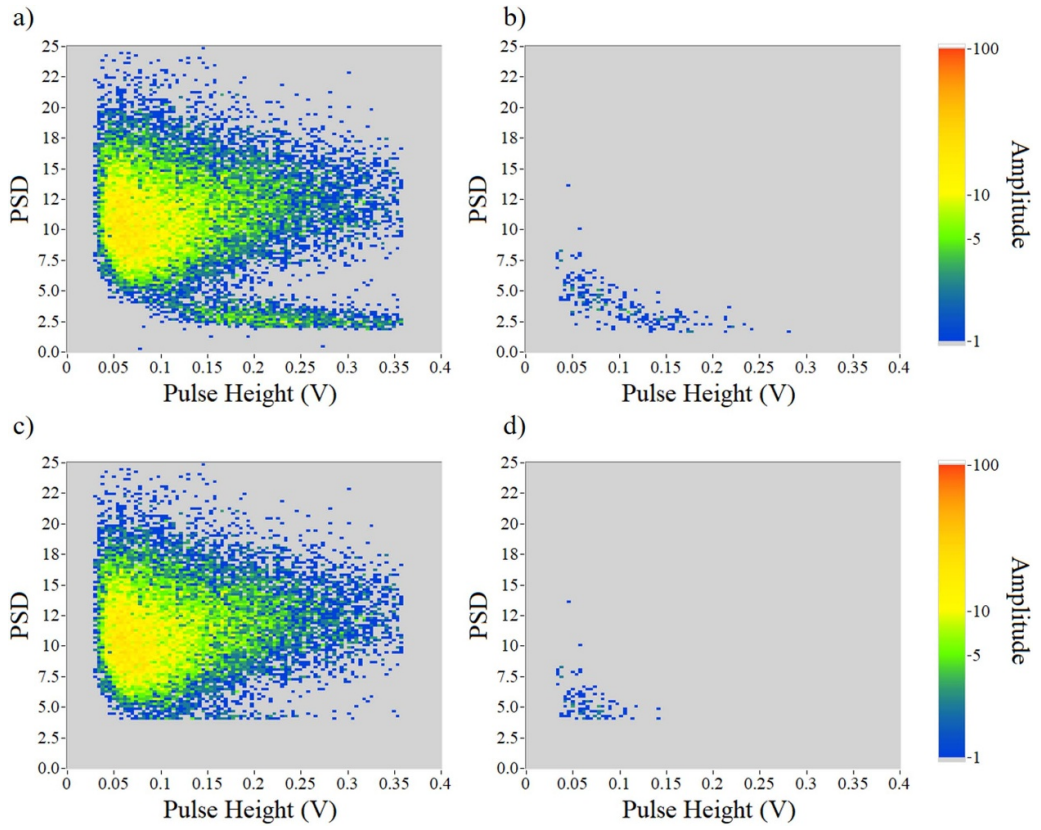


**Figure 8.** PSD histograms measured on (a) $^{241}$Am-Be neutron/gamma source and (b) $^{60}$Co gamma source, as in figure 6, displaying only events classified as neutrons using the FBM technique illustrated in figure 7. (c) and (d) show the same data with an additional PSD cut applied at 4.

detector characterisation facility. To correct for this, a background measurement was performed by removing the gamma source. The fraction of incident gammas that were accepted, $C_\gamma$, after background counts, $C_B$, were subtracted was used to calculate the gamma sensitivity, $\eta_\gamma$, of the detector:

$$\eta_\gamma = \frac{(C_\gamma - C_B)}{2A}\frac{4\pi d^2}{l^2}, \tag{3}$$

where A is the activity of the gamma source, $d$ the distance from source to scintillator, and $l^2$ the detector active area, 16 mm×16 mm. The factor of two is included in the denominator as the most frequent $^{60}$Co decay (99.88%) emits two gammas:

$$^{60}\mathrm{Co} \rightarrow ^{60}\mathrm{Ni} + \beta\,(0.31\mathrm{MeV}) + \gamma\,(1.173\mathrm{MeV}) + \gamma\,(1.333\mathrm{MeV})\,. \tag{4}$$

With the filtration settings shown in table 1, the gamma sensitivity of this detector is calculated to be $8.5\times10^{-6}$. This is highly promising, as gamma sensitivity levels $< 1\times10^{-5}$ are typically required for neutron detectors in scattering applications [22].

Lower values for gamma sensitivity can be achieved by increasing the neutron acceptance threshold, or the integrated charge cut, however this results in a lower neutron detection efficiency as true neutron events are also rejected. In practice, signal processing settings are often optimised for maximum neutron detection efficiency at the highest acceptable level of gamma sensitivity.

*3.2.2. Gamma rejection—beamline performance.* Acceptable levels of gamma sensitivity in neutron scattering applications are dependent on the specific experimental conditions. The most stringent requirements arise when measuring small, weakly scattering samples, as in these cases the gamma flux on the detector can exceed the neutron flux by several orders of magnitude.

To investigate the suitability of the nanoscintillator for use in neutron scattering applications, the detector was studied in an experimental configuration designed to generate an incident

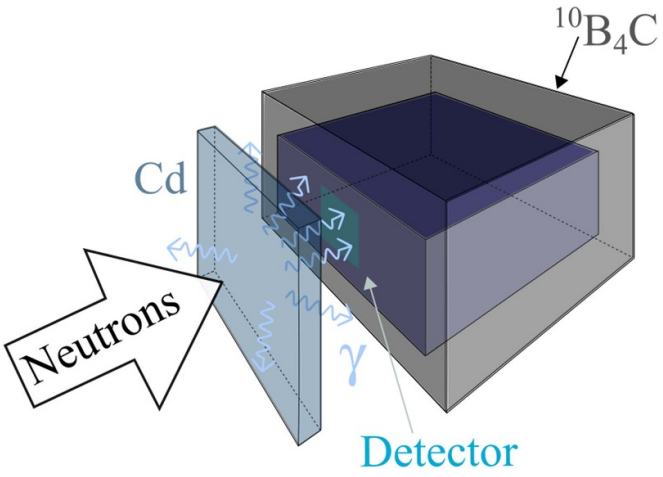


**Figure 9.** Illustration of the experimental set up used to verify the gamma rejection capabilities of the detector in a realistic setting.

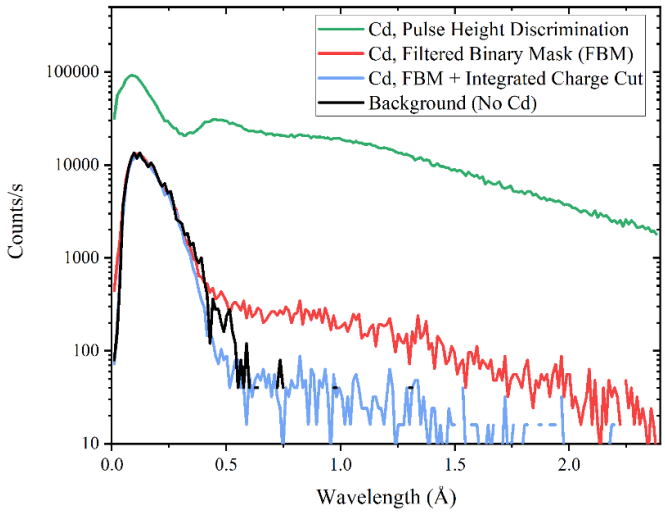


**Figure 10.** Wavelength spectra measured using different signal processing for the experimental set-up illustrated in figure 9.

gamma flux higher than most typical neutron scattering experiments. A sketch of the experimental set up is illustrated in figure 9. Firstly, the detector was surrounded with $^{10}B_4C$ to remove incident neutrons, and the background spectra measured. 480 keV gammas are generated by the $^{10}B$ neutron absorption, however as these are over 2 times lower energy than $^{60}Co$ gammas, they can be easily rejected in the signal processing. A 1 mm thick layer of Cd was then placed in front of the detector, in the direct neutron beam, to produce a large gamma flux and test the practical gamma rejection capabilities of the detector and the signal processing methods employed. At wavelengths >0.56 Å, over 99.99% of the incident neutrons are absorbed by 1 mm of Cd. The absorption of neutrons causes the emission of a range of high energy gammas on the order of several MeV [47]. 10 ms frames, triggered on the synchrotron $t_0$ pulse, were recorded and post processed to extract the time of arrival of events and reconstruct the time of flight spectra.

The background neutron spectrum that was measured with the detector shielded by $^{10}B_4C$, without the Cd plate, is shown by the black curve in figure 10. A portion of fast neutrons with wavelengths <0.5 Å are transmitted through the $^{10}B_4C$ and measured. At wavelengths > 0.5 Å, a very small number of events are measured. The green, red, and blue curves in figure 10 show the spectra measured with the gamma generating Cd in place, for different PSD techniques. For the green curve, discrimination is based solely on the pulse height of the analogue signal. This is the equivalent of counting all the events shown in figure 6(a), and results in the detection of $1.8\times10^4$ events per second at 1 Å, of which the vast majority are Cd generated gammas.

Introducing the FBM discrimination technique (as in figure 8(a)) reduces the number of events measured by a factor of 90 (for $\lambda$ >0.5 Å), as shown by the red curve in figure 10. This technique alone is successful in eliminating a large portion of the gamma signals, however the number detected is significantly above background levels. When including the normalised integrated charge cut (as in figure 8(c)), gamma sensitivity is further reduced by a factor of 5, as shown by the blue curve in figure 10. In this case the gamma sensitivity is within statistical error of the background spectra measured as the data is limited by low counting statistics. While this experiment is not designed to give quantitative values, the level of gamma sensitivity shown is in agreement with the value measured in section 3.2.1. This confirms the signal processing techniques shown are appropriate for use in many neutron scattering experiments.

### 3.3. Neutron scintillation decay time

Figure 11 shows the average neutron signal measured at low rates on the $^{241}$Am-Be source for both the ZnS:Ag/$^6$LiF nanoscintillator (blue), and the microscintillator (red). Peak intensity is normalised to one in order to compare the decay profiles. Neutron signals were separated from gammas and PMT noise using the PSD method described in section 3.2, with the filtration settings and thresholds adjusted accordingly for the microscintillator. The average gamma signals are not shown because dim gamma scintillation events could not be separated from the response to gammas interacting directly in the PMT.

The average signals in figure 11 were fitted to two exponentials and one hyperbolic decay, given in equation (5):

$$y = a\exp\left(-\frac{\tau}{t_1}\right) + b\exp\left(-\frac{\tau}{t_2}\right) + \frac{c}{(1+\tau/t_3)^n}, \quad (5)$$

where $a$, $b$ and $c$ are the amplitudes of the two exponential and hyperbolic decays respectively. $n$ is a fitting constant usually close to one that accounts for the presence of multiple traps in realistic phosphors; for the decays shown, $n = 1.15$. The exponential decay time constants ($t_1$, $t_2$) describe prompt excitonic recombination while the hyperbolic decay time $t_3$ is associated with afterglow [34, 48, 49]. Fitted values of decay time constants and time to decay to certain percentages of the maximum signal are shown in table 2.

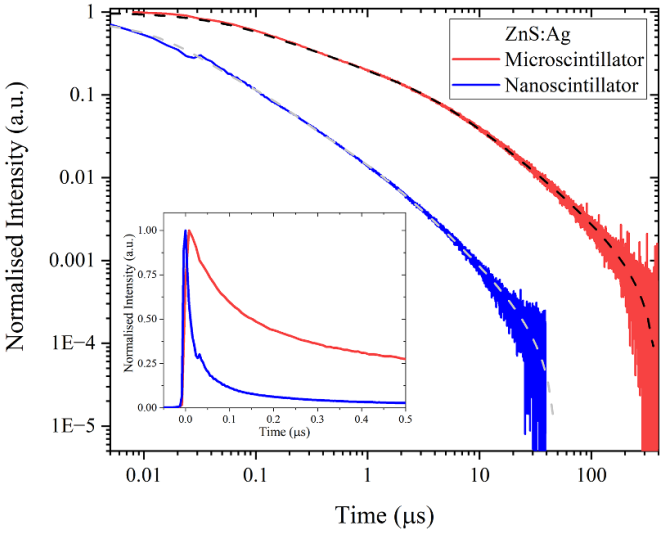


**Figure 11.** Normalised average neutron signal from ZnS:Ag/$^6$LiF nanoscintillator (blue) and microscintillator (red). Dashed curves show fitted decay profile. Fitting parameters and time to decay to different proportions of peak signal (37%, 10%, 1%, 0.1%) are given in table 2. Insert shows the first 500 ns of decay with linear axes.

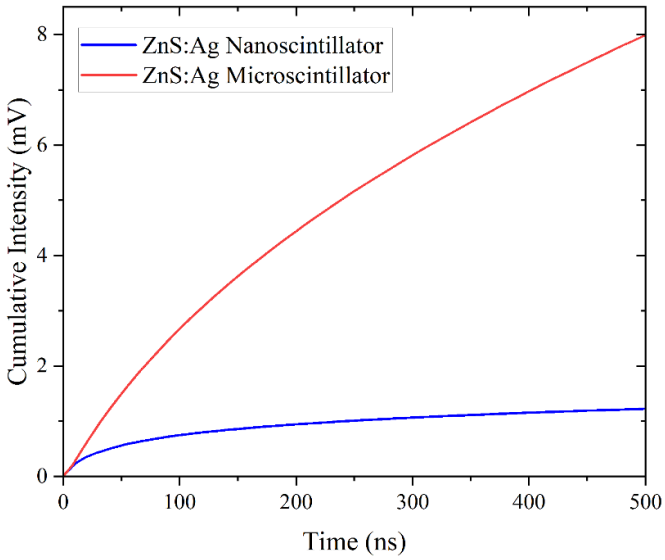


**Figure 12.** Cumulative intensity of measured light output ($y = \int_0^t I(t)\mathrm{d}t$) for average neutron signals measured with the ZnS:Ag/$^6$LiF nanoscintillator (blue) and the microscintillator (red).

**Table 2.** Fitted time constants and measured decay times for averaged neutron signals measured using the ZnS:Ag/$^6$LiF nanoscintillator, and ZnS:Ag/$^6$LiF microscintillator for comparison. Relative amplitudes of decay components are given in brackets.

| | | Nano Response | Micro Response |
|---|---|---|---|
| Fitted Time Constant (Amplitude) | $t_1$ | 7.88 ± 0.03 ns (0.57) | 73.0 ± 0.2 ns (0.45) |
| | $t_2$ | 43.6 ± 0.4 ns (0.27) | 314.8 ± 0.9 ns (0.27) |
| | $t_3$ | 129 ± 2 ns (0.17) | 2164 ± 2 ns (0.29) |
| Decay Time to: | 1/e | 18 ± 4 ns | 285 ± 8 ns |
| | 10% | 0.114 ± 0.008 μs | 3.15 ± 0.5 μs |
| | 1% | 1.39 ± 0.2 μs | 36 ± 1 μs |
| | 0.1% | 8.8 ± 0.5 μs | 190 ± 40 μs |

The measured average decay to 10%, 1% and 0.1% was 20–30 times faster in the nanoscintillator, and the primary decay was measured to be 16 times faster than in the standard microscintillator. The fitted decay times indicate that all components of the scintillation are occurring on shorter timescales in the nanoscintillator. The effect of afterglow mechanisms on the overall luminescence behaviour are significantly reduced, as shown by the reductions in amplitude (from 29% to 17%) and decay time (from 2.16 μs to 129 ns) of the hyperbolic component. Possible reasons for faster decay in the nanoparticle scintillator, including reduced separation of traps and luminescence centres, and strongly localised excitons, are discussed in Mann *et al* [37]. This previous work reports the timing properties of alpha scintillation of the nanoparticle powder, as opposed to the neutron response of the scintillator screens shown here. Absolute values for decay times vary due to differences in the experimental configuration, penetration depth of the neutron and ionisation densities of the $^3$H and $^4$He reaction products. However, the ratio between nanoparticle and microparticle scintillation timings are consistent in both works.

Figure 12 shows the cumulative intensity of light output as a function of time for the ZnS:Ag/$^6$LiF nanoscintillator and microscintillator detectors. Unlike figure 11, the average signal intensity was not normalised to one, which allows for a direct comparison of the light output and collection from both scintillators. Integrating over the first 500 ns, 6.6 times less light was measured from the nanoscintillator. This difference increases with time, as the microscintillator emission is dominated by long lifetime components; over 5 μs, 14 times less light was measured from the nanoscintillator. It is worth noting that the quantum efficiency of the PMT used (shown in figure 4) is a better match to the emission spectrum of the microscintillator, which is peaked at 450 nm. When correcting for the quantum efficiency of the PMT, the nanoscintillator emits approximately a factor of 2 times less light over 500 ns than the commercial scintillator. Optimising light output and collection is important in scintillation detectors as it can have a direct impact on detection efficiency. If insufficient light is measured, neutron events will not be counted. When constructing position sensitive detectors, the additional components involved (such as wavelength shifting fibres, light guides, diffusers etc) typically lead to much further light loss. Therefore, achieving the maximum light output from the scintillator, ideally at wavelengths with efficient photodetectors, will be a significant priority for future development.

### *3.4. Rate capability*

To assess the rate capability of the detector, a series of 16 ms traces were recorded, while an increasingly larger area of the detector was exposed to the incident neutron flux of the CRISP beamline. The incident rate was controlled by changing the neutron beam width using neutron absorbing slits which were positioned 280 mm in front of the detector. The vertical slits were set to 10 mm and the horizontal slits were increased

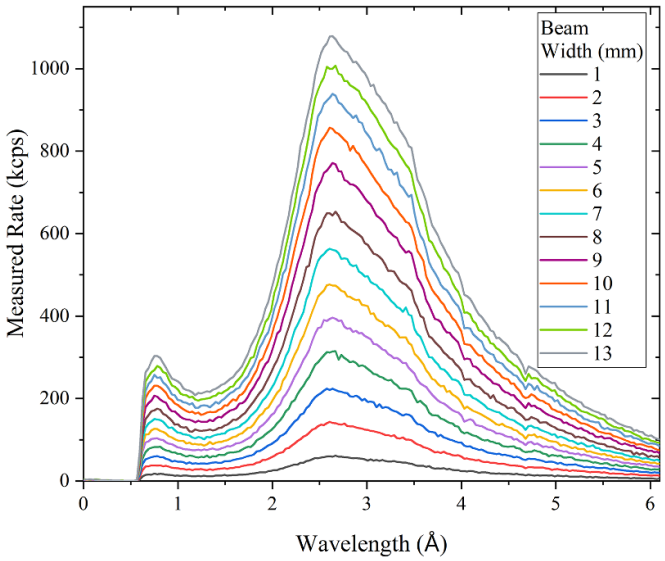


**Figure 13.** Neutron wavelength spectra of the CRISP beamline at ISIS measured using the nanoscintillator detector for different incident neutron rates.

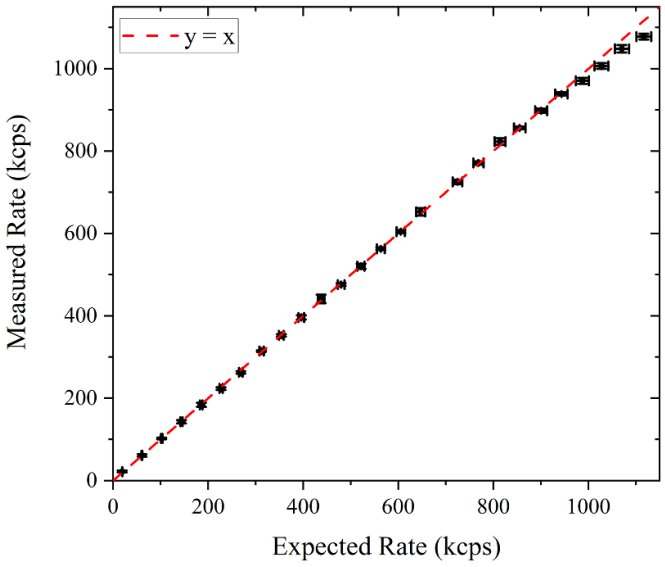


**Figure 14.** Measured rate at 2.6 Å as a function of expected rate for increasing incident neutron flux. Rate data is taken from figure 13. The dashed line indicates $y = x$ as a guide to the eye.

in 0.5 mm steps to vary the beam width from 0.5–13 mm. Neutron wavelength spectra measured with the nanoscintillator detector for different neutron rates are shown in figure 13. Every other spectra is excluded from this plot for clarity. For all incident fluxes, the neutron spectra show the characteristic shape of the liquid hydrogen moderator viewed by the CRISP beamline. (200) and (111) aluminium Bragg edges are visible at 4.03 Å and 4.68 Å respectively, primarily originating from vacuum windows and neutron beam monitors in the neutron flight path. There is no visible distortion or saturation in the neutron spectra with increasing flux.

Figure 14 shows measured peak rates at 2.6 Å as a function of expected rate. The dashed line indicates ideal performance with no rate limitation, and this is in very close agreement with the measured values from the nanoscintillator detector. At rates above 1Mcps slight deviation from linearity is seen which may be initial signs of some rate limitation due to deadtiming. The measured count loss at 1.12 Mcps is 3.5%. This represents an improvement of approximately 70 times over current ZnS:Ag/$^{6}$LiF scintillation detector technology, which exhibit 10% deadtiming at 16 kcps.

As only minimal deadtiming is seen at rates of 1.1 Mcps, and the neutron spectra in figure 13 are not stunted, the saturation point of the detector is likely significantly higher than it was possible to measure in these tests. Potential count rate capabilities were investigated by inspecting signals from the highest rate regions of time of flight spectra. Figure 15 shows an example of the analogue signal measured at high incident rates (black) and the filtered signal (blue), with counted neutrons indicated by red crosses.

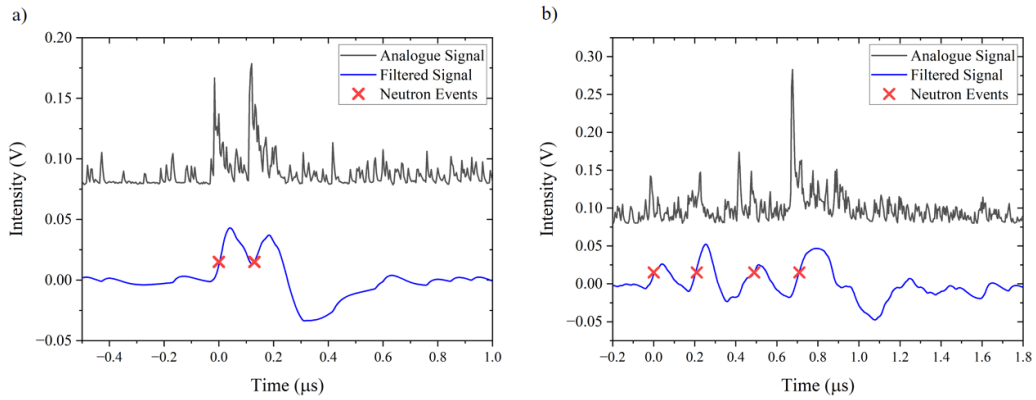


**Figure 15.** Examples of the analogue (black) signals measured in high rate regions and the corresponding FBM signal (blue). Crosses indicate the trigger time of events determined to be neutrons.

Two neutrons arriving 130 ns apart are resolved in figures 15(a), and (b) shows four neutrons that are detected within 1 $\mu$s. These traces imply that rate capabilities much greater than the 1.1 Mcps seen in figure 14 should be achievable with nanoparticle ZnS:Ag/$^6$LiF and this signal processing technique. Future work will include determining the absolute rate capabilities of this system by improving the efficiency and area of the nanoscintillator, or by utilising a higher flux neutron source.

## 4. Conclusions

The first thermal neutron scintillator using nanoparticle ZnS:Ag has been developed and shown to have potential for use in high count rate neutron detection applications. Pulse shape differences between neutron and gamma induced scintillation signals were demonstrated in nanoparticle ZnS:Ag/$^6$LiF. These differences can be exploited to achieve good neutron-gamma discrimination capabilities; gamma sensitives of $8.5 \times 10^{-6}$ to $^{60}$Co gammas were obtained with simple signal processing techniques. This level of gamma sensitivity would be acceptable for use in many applications at neutron scattering facilities, and there is opportunity to improve gamma rejection capabilities with optimisation of signal processing parameters. The gamma rejection capabilities were equally effective when tested at high rates on the EMMA beamline at ISIS. The spectrum measured with high incident gamma flux was within statistical errors of background measurements. The results shown in this work were obtained by post-processing saved data, however real time signal processing is currently under development and will be implemented in the next detector prototype.

Neutron scintillation in nanoparticle ZnS:Ag/$^6$LiF is shown to occur on fast timescales; the average primary decay time was measured to be less than 20 ns. The average signal decays to 0.1% of its peak intensity in less than 10 $\mu$s, 20 times faster than micron sized ZnS:Ag/$^6$LiF. This fast decay and reduction of afterglow allows nanoparticle ZnS:Ag/$^6$LiF to attain much higher count rate capabilities than standard ZnS:Ag/$^6$LiF based detectors. Rate capabilities of 1.1Mcps with less than 5% deadtiming were measured for a single readout channel. These rate capabilities are almost 70 times higher than is achievable with the current standard of ZnS:Ag/$^6$LiF scintillation detectors. Inspection of high rate regions in recorded signals show instances of successive neutrons resolved in within 250 ns. These examples suggest rate capabilities well over 1 Mcps per readout channel may be achievable with nanoparticle ZnS:Ag/$^6$LiF scintillators.

Although these initial results are highly promising, further work is needed to develop nanoparticle ZnS:Ag/$^6$LiF into a viable replacement for standard ZnS:Ag/$^6$LiF detectors. Measurements of light output and collection show 6.6 times less light was detected in the first 500 ns of nanoparticle emission compared to the standard ZnS:Ag/$^6$LiF scintillator. Over 5 $\mu$s, the difference increases to a factor of 14. Low light output and collection can limit detection efficiency, as dimmer neutron events may not be counted. In future work, the detection efficiency of the nanoparticle detector will be assessed, and efforts made to improve the light yield from the nanoparticle scintillator. This will involve investigating the effects of synthesis parameters, including capping agents and co-dopants on the optical properties of the nanoparticles. The impact of nanoparticle size and morphology on the luminescence behaviour will also be studied. Improvements to the light output and collection in the whole detector system will additionally be pursued by optimising scintillator composition and employing alternative photodetectors. In addition to benefiting detection efficiency, increased light detection would improve neutron-gamma discrimination capabilities, further reducing gamma sensitivity.

While some limitations remain, the demonstration of PSD is an important step in the advancement of nanoparticle ZnS:Ag/$^6$LiF neutron detectors for use in high gamma background environments such as neutron scattering facilities. With count rate capability on the order of 70 times greater than

current ZnS:Ag/$^{6}$LiF scintillators, nanoparticle ZnS:Ag/$^{6}$LiF show exciting potential for development into future high rate capability neutron detectors.

## Data availability statement

The data cannot be made publicly available upon publication because they are not available in a format that is sufficiently accessible or reusable by other researchers. The data that support the findings of this study are available upon reasonable request from the authors.

## Acknowledgments

This work was funded by the Science and Technology Facilities Council (STFC) through the ISIS department. The authors thank Dr Sarah Youngs for support synthesising nanoparticles, Mr John Dreyer for producing the mechanics which contained the detector, and Dr Gavin Stenning for assisting with XRD measurements in the ISIS Materials Characterisation Laboratory.

## ORCID iDs

Sarah E Mann https://orcid.org/0000-0002-3905-0393
Giacomo Mauri https://orcid.org/0000-0002-8711-630X
G Jeff Sykora https://orcid.org/0000-0003-0396-8618

## References

[1] Peerani P *et al* 2012 Testing on novel neutron detectors as alternative to $^{3}$He for security applications *Nucl. Instrum. Methods Phys. Res.* A **696** 110–20
[2] Pietropaolo A *et al* 2020 Neutron detection techniques from $\mu$eV to GeV *Phys. Rep.* **875** 1–65
[3] Vogel S and Carpenter J 2012 Brief introduction to neutron scattering and global neutron user facilities *J. Miner. Met. Mater. Soc.* **64** 104–11
[4] ISIS Neutron and Muon Source 2024 (available at: www.isis.stfc.ac.uk) (Accessed February 2024)
[5] Institut Laue-Langevin (available at: www.ill.eu/) (Accessed February 2024)
[6] NIST Center for Neutron Research (available at: www.nist.gov/ncnr) (Accessed February 2024)
[7] Spallation Neutron Source (available at: https://neutrons.ornl.gov/sns) (Accessed February 2024)
[8] Japan Proton Accelerator Research Complex - MLF (available at: https://mlfinfo.jp/en/aboutmlf/) (Accessed February 2024)
[9] China Spallation Neutron Source (available at: http://english.ihep.cas.cn/csns/) (Accessed February 2024)
[10] Andersen K and Argyriou D *et al* 2020 The instrument suite of the European spallation source *Nucl. Instrum. Methods Phys. Res.* A **957** 163402
[11] Qian S *et al* 2022 CENTAUR-the small- and wide-angle neutron scattering diffractometer/spectrometer for the second target station of the spallation neutron source *Rev. Sci. Instrum.* **93** 075104
[12] ISIS Neutron and Muon Source 2024 *Next steps for ISIS-II and the Endeavour programme* (available at: www.isis.stfc.ac.uk/Pages/Next-Generation-Capabilities-for-the-ISIS-Neutron-and-Muon-Source.aspx) (Accessed February 2024)
[13] Lagrange J B *et al* 2019 Progress on design studies for the ISIS II upgrade *10th Int. Particle Accelerator Conf.*
[14] Sykora G J, Schooneveld E M, Rhodes N J and Van Eijck L 2012 Gamma sensitivity of a ZnS:Ag(6-LiF) wavelength shifting fiber neutron detector in mixed neutron-gamma fields *IEEE Nuclear Science Symp. Conf. Record* pp 1567–71
[15] Chong S, Riedel R, Funk L, Visscher T, Donahue C, Hannan B, Montcalm C, Beal J and Hayward J 2022 The development of a $^{6}$Li-based pixelated neutron detector for neutron reflectometry at the spallation neutron source *Nucl. Instrum. Methods Phys. Res.* A **1039** 167052
[16] Pooley D, Lee J, Brouard M, John J, Kockelmann W, Rhodes N, Schooneveld E, Sedgwick I, Turchetta R and Vallance C 2017 Development of the 'GP2' detector: modification of the PImMS CMOS sensor for energy resolved neutron radiography *IEEE Trans. Nucl. Sci.* **64** 2970–81
[17] Mauri G, Sykora G J, Schooneveld E M and Rhodes N J 2021 Enhanced position resolution for ZnS:Ag/$^{6}$LiF wavelength shifting fibre thermal neutron detectors *Eur. Phys. J. Plus* **136** 286
[18] Raspino D, Rhodes N J and Schooneveld E M 2015 A large area neutron detector array for the LET instrument at ISIS *IEEE Nuclear Science Symp. and Medical Imaging Conf. (NSS/MIC)* pp 1–4
[19] Keen D, Gutmann M and Wilson C 2006 SXD-the single-crystal diffractometer at the ISIS spallation neutron source *J. Appl. Crystallogr.* **39** 714–22
[20] Sykora G J, Schooneveld E M and Rhodes N J 2015 Large area wavelength shifting fibre thermal neutron detectors using 64 channel flat panel PMTs *IEEE Nuclear Science Symp. and Medical Imaging Conf., NSS/MIC 2015*
[21] Hurd A and Kouzes R 2014 Why new neutron detector materials must replace helium-3 *Eur. Phys. J. Plus* **129** 1–3
[22] Zeitelhack K 2012 Search for alternative techniques to helium-3 based detectors for neutron scattering applications *Neutron News* **23** 10–13
[23] Rhodes N, Schooneveld E and Eccleston R 2004 Current status and future directions of position sensitive neutron detectors at ISIS *Nucl. Instrum. Methods Phys. Res.* A **529** 243–8
[24] Sakasai K, Nakamura T, Katagiri M, Soyama K, Birumachi A, Satoh S, Rhodes N and Schooneveld E 2009 Development of neutron detector for engineering materials diffractometer at J-PARC *Nucl. Instrum. Methods Phys. Res.* A **600** 157–60
[25] Katagiri M, Nakamura T, Ebine M, Birumachi A, Sato S, Shooneveld E M and Rhodes N J 2007 High-position-resolution neutron imaging detector with crossed wavelength shifting fiber read-out using two ZnS/$^{6}$LiF scintillator sheets *Nucl. Instrum. Methods Phys. Res.* A **573** 149–52
[26] Wang C L 2016 Performance improvements of wavelength-shifting-fiber neutron detectors using high-resolution positioning algorithms *Rev. Sci. Instrum.* **87** 053303
[27] Wang C L and Riedel R A 2016 Improved neutron-gamma discrimination for a $^{6}$Li-glass neutron detector using digital signal analysis methods *Rev. Sci. Instrum.* **87** 013301
[28] Rofors E *et al* 2021 Response of a Li-glass/multi-anode photomultiplier detector to collimated thermal-neutron beams *Nucl. Instrum. Methods Phys. Res.* A **999** 165170
[29] Ishikawa A *et al* 2022 Evaluation of the thermal neutron sensitivity, output linearity and gamma-ray response of optical fiber-based neutron detectors using li-glass

scintillator *Nucl. Instrum. Methods Phys. Res.* A **1025** 166074
[30] Loyd M *et al* 2024 Sub-millimeter resolution SiPM-based neutron anger camera *Nucl. Instrum. Methods Phys. Res.* A **1058** 168871
[31] Sykora G J, Schooneveld E M and Rhodes N J 2018 ZnO:Zn/$^{6}$LiF scintillator-a low afterglow alternative to ZnS:Ag/$^{6}$LiF for thermal neutron detection *Nucl. Instrum. Methods Phys. Res.* A **883** 75–82
[32] Mann S, Schooneveld E, Rhodes N, Liu D and Sykora G 2023 Position sensitive ZnO:Zn neutron detector - a high count rate alternative to ZnS:Ag scintillation detectors *Nucl. Instrum. Methods Phys. Res.* A **1057** 168716
[33] van Eijk C, Bessière A and Dorenbos P 2004 Inorganic thermal-neutron scintillators *Nucl. Instrum. Methods Phys. Res.* A **529** 260–7
[34] McKeever S 1985 Tunnelling and anomalous fading *Thermoluminescence of Solids* (Cambridge University Press) pp 143–8
[35] Richards S, Sykora G and Taggart M 2021 High count rate pulse shape discrimination algorithms for neutron scattering facilities *Nucl. Instrum. Methods Phys. Res.* A **989** 164946
[36] Warburton W K, Carlson J S and Feng P L 2021 Organic glass scintillator (OGS) property comparisons to Stilbene, EJ-276 and BC-404 *Nucl. Instrum. Methods Phys. Res.* A **1018** 165778
[37] Mann S E, Schooneveld E M, Rhodes N J, Liu D and Sykora G J 2023 Timing properties of radioluminescence in nanoparticle ZnS:Ag scintillators *Opt. Mater.* X **17** 100226
[38] Abdalla A M, Ali A M, Al-Jarallah M, Okada G, Kawaguchi N and Yanagida T 2019 Radon detection using alpha scintillation KACST cell *Nucl. Instrum. Methods Phys. Res.* A **922** 84–90
[39] Ramazani-Moghaddam A and Mojiri-Forooshani R 2019 Preparation of nanocomposite scintillator of ZnS doped with Ag, Cu and AgCu for alpha particle detection *J. Nanostruct.* **9** 556–62
[40] Li Q H, Lin S P, Ma D C and Wang B 2019 Photoluminescence properties and threshold effect of ZnS:Ag nanoparticles synthesized by a hydrothermal process *Int. J. Mod. Phys.* B **33** 1950027
[41] Wu Y, Shao Y and Jacobsohn L G 2020 Luminescence of ZnS:Ag scintillator prepared by the hydrothermal reaction method: effects of reaction temperature and time, Ag concentration and co-doping with Al *Opt. Mater.* **107** 110015
[42] Chadwick M *et al* 2006 ENDF/B-VII.0: next generation evaluated nuclear data library for nuclear science and technology *Nucl. Data Sheets* **107** 2931–3118
[43] Cazzaniga C, Raspino D, Sykora G J and Frost C D 2021 Dosimetry of thermal neutron beamlines at a pulsed spallation source for application to the irradiation of microelectronics *IEEE Trans. Nucl. Sci.* **68** 921–7
[44] Piscitelli F *et al* 2018 Characterization of the Multi-Blade 10B-based detector at the CRISP reflectometer at ISIS for neutron reflectometry at ESS *J. Instrum.* **13** P05009
[45] Thomason J 2019 The ISIS spallation neutron and muon source-the first thirty-three years *Nucl. Instrum. Methods Phys. Res.* A **917** 61–67
[46] Warren B E 1990 *Particle Size Broadening, in: X-Ray Diffraction* (Dover Publications Inc.) pp 251–4
[47] Bondar B, Gorbachenko O, Leshchenko B, Kadenko I, Plujko V and Solodovnyk K 2021 Gamma-ray spectrum from Cd induced by fast neutrons in indoor experiments *Nucl. Phys.* A **1010** 122192
[48] Nakazawa E 2007 *Phosphor Handbook* (CRC Press)
[49] Visocekas R, Ceva T, Marti C, Lefaucheux F and Robert M C 1976 Tunneling processes in afterglow of calcite *Pysica Status Solidi* a **35** 315–27